JOURNAL OF Applied Polymer SCIENCE

Role of Crystalline Ethylene-Propylene Copolymer on Mechanical Properties of Impact Polypropylene Copolymer

Wonchalerm Rungswang, Phutsadee Saendee, Boonyakeat Thitisuk, Thipphaya Pathaweeisariyakul, Watcharee Cheevasrirungruang

Technical and Research Division, Thai Polyethylene Co., Ltd., Siam Cement Group (SCG), Muang, Rayong 21150, Thailand

Correspondence to: W. Rungswang (E-mail: wonchalr@scg.co.th)

ABSTRACT: Impact polypropylene copolymer (IPC) has been known as a multiphase material in which an ethylene-propylene (EP) random copolymer, serves as toughening component, is dispersed in the homo-polypropylene hPP matrix. The crystalline EP copolymer (cEP) is another component whose role and microstructural effect on the IPC properties has not been well understood. This work reveals the relationship between the microstructure of cEP and the mechanical properties, that is, impact and tensile resistance, of IPC. We clarify that IPC comprising high contents of cEP with long homo-PP segment can extend the elongation at break while cEP with high content of homo-PE segment contributes to high impact strength. Mechanisms for both of these processes have been proposed. © 2012 Wiley Periodicals, Inc. J. Appl. Polym. Sci. 000: 000–000, 2012

KEYWORDS: copolymers; mechanical properties; polyolefins; morphology

Received 17 July 2012; accepted 21 August 2012; published online
DOI: 10.1002/app.38495

INTRODUCTION

Polypropylene (PP) is one of the most widely used commodity plastics due to the excellent mechanical properties, such as heat resistance, high strength, processability, and also low cost. However, PP has low impact strength, especially at low temperatures which is its major limitation.[1,2] Thus, several approaches to improve its toughness have been used, for example, reducing crystal size by adding nucleating agent,[3] blending with elastomer, and copolymerizing with α-olefinic species.[4–7] Among several techniques, *in situ* copolymerization with ethylene by adding a gas-phase reactor in the production line is an effective one which has been used on an industrial scale to obtain high-impact resistant PP or impact PP copolymer (IPC).[8–10]

In the gas-phase reactor, several types of ethylene-propylene (EP) copolymers have been produced. EP random copolymer (EPR) is a major component which is responsible for the toughness improvement.[11,12] Furthermore, several segmental PE and PP block copolymers with segment lengths long enough to form crystalline structure, so-called crystalline E-P copolymer (cEP), have also been produced. cEP is a mixture of block homo-PP and homo-PE connected with random E-P segments (rEP) in various composition distributions and chain lengths.[13,14] When IPC is melted, a unique heterophasic morphology is formed. A widely accepted model for IPC morphology states that EPR forms a droplet as dispersed phase in the homo-PP (hPP) matrix and at the EPR-PP interphase cEP with long homo-PP segments (or PP-rich) outwardly aligns the homo-PP segment to the hPP matrix. Whereas for cEP with long homo-PE segment, it might form a PE-rich core in the EPR droplet and outwardly aligns its rEP segment to the EPR shell.[15,16]

Mechanical properties, such as impact strength, flexural modulus, and tensile-fracture properties, are the major concern for IPC products, especially in automotive and electrical-appliance uses, and a trend for IPC development is in enhancing those properties based on polymer microstructure. Thus, the relationship between the mechanical properties and the microstructure of each component is needed to be clearly understood. It is well known that the EPR is responsible for the toughness enhancement, and the hPP contributes to the rigidity of the IPC. However, there are just a few reports mentioned on the role of cEP. Tan et al. reported that the impact strength of IPC can be remarkably improved from 11.6 to 48.2 kJ/m^2 by increasing the cEP content from 5.34 to 17.81%. This might result from better adhesion between the EPR droplet and hPP matrix.[17] Zhang et al. also revealed that cEP suppresses the glass transition temperature (T_g) when comparing blended and neat EPR. Furthermore, they also showed that a co-crystallization of homo-PP-cEP segments and the hPP matrix can occur in cEP/hPP blends.[15] This confirms that the cEP molecules have an

Additional Supporting Information may be found in the online version of this article.

Table I. Impact Strength and Tensile Fracture Properties of IPC Samples

	Mechanical Properties				
		Tensile-fractured properties			
Samples	Impact strength (kJ/m^2)	Elongation at yield (%)	Stress at yield (MPa)	Elongation at break (%)	Stress at break (MPa)
IPC-A	24.1 ± 1.8	7.16 ± 0.27	29.0 ± 0.4	88.9 ± 15.0	18.8 ± 1.5
IPC-B	26.3 ± 2.2	5.81 ± 0.32	25.8 ± 0.2	59.2 ± 9.8	17.9 ± 0.1
IPC-C	24.9 ± 2.0	5.80 ± 0.14	26.0 ± 0.3	43.5 ± 3.7	19.2 ± 0.4

interaction with both hPP and EPR molecules, which leads to an improvement in compatibility between the hPP and EPR phases. Song et al.[18,19] also showed that shear-enhanced crystallization could occur only in the presence of cEP and could not be observed in hPP/EPR blend. These findings are significant because they confirm that cEP can affect the properties of IPC from molecular to macroscopic level. However, the role of the microstructure of cEP on the mechanical properties of IPC has yet to be clarified.

Here, three IPC samples which exhibit different mechanical properties, that is, impact and tensile resistances, were selected as case studies. The IPC samples studied were separated into the components EPR, hPP, and cEP, and their individual microstructures were elucidated in detail. The differences between each component microstructure, especially cEP, were related to the mechanical properties, including proposed mechanisms.

EXPERIMENTAL

Materials

IPC samples were supplied by Thai Polyethylene Co., Ltd, Rayong, Thailand. Acetone, n-decane, n-heptane, and butylated hydroxytoluene were purchased from Sigma Aldrich, Singapore. Acetone was obtained from Merck, Germany. All chemicals were used without further purification.

Characterization

Impact strengths of IPCs were evaluated by CEAST universal pendulum followed standard method ISO 180:2000(E) (Determination of Izod Impact Strength). Tensile-fracture properties were tested by universal testing machine (INSTRON) at 500 mm/min of tensile speed. For the preparation of impact and tensile testing specimens, the IPC pellets were melted at 230°C and injected into cooled molds which notched-bar and dog-bone specimens were obtained for impact and tensile tests, respectively. The samples were left for 2 days at 25°C before testing at this temperature. Pentad of E-P sequence was evaluated by carbon-13 nuclear magnetic resonance spectroscopy (^{13}C NMR), using a high-resolution ^{13}C-NMR Bruker DRX 500 spectrometer. The samples were measured at 125°C in benzene-D6 with 90° of pulse angle and 12 s of pulse interval. Weight-average (M_w) and number-average molecular weight (M_n) were measured by gel permeable chromatography (GPC), Polymer Laboratories (Agilent), model PL-GPC 220. 1,2,4-trichlorobenzene (TCB) containing 0.025% wt of Santonox as an antioxidant was used as mobile phase with 1.0 cm^3/min of flow rate at 160°C. Short-chain-branch (SCB) frequency was measured by GPC-IR5 (Polymer Char, Valencia, Spain) which TCB was used as mobile phase with 0.5 cm^3/min of flow rate at 140°C of column temperature. A calibration curve for SCB determination was prepared from PE with known content of octane-1 comonomer. Thermal profiles were measured by differential scanning calorimeter (DSC) (DSC 823 METTLER TOLEDO) under N_2 atmosphere. The samples were first heated to 200°C at 10°C/min of heating rate to erase the thermal history, then cooled down to 50°C at 10°C/min of cooling rate. Finally, the samples were heated to 200°C at 10°C/min of heating rate to obtain the DSC thermogram. Thermal fractionation through successive self-nucleation and annealing (SSA) was conducted to determine a segmental length of homo-PE segment in cEP. The cEP sample was heated to 200°C and hold for 5 min to erase the thermal history. Then, the sample was cooled down to 25°C at 10°C/min of cooling rate. Subsequently, the temperature was raised to 180°C which is a selected SSA temperature (Ts_1). After isothermally retaining at this temperature for 5 min, the sample was cooled down to 25°C at 10°C/min of cooling rate to complete an annealing cycle. Then, the sample was heated to Ts_2 which is 5°C lower than previous T_s. The annealing cycle was repeatedly proceeded to 50°C followed by heating ramp at 10°C/min of heating rate to obtain the thermogram. To observe EPR size and its dispersion, tensile specimens were fractured in liquid N_2 before etching in xylene at room temperature for 12 h. After drying for 24 h at room temperature, the specimens were coated with gold before observation by scanning electron microscope (SEM) (Quanta 250, FEI). EPR diameter and its distribution were evaluated by Image J software with 100 counts from three different micrographs. Wide angle X-ray diffraction (WAXD) measurements were conducted at Synchrotron Light Research Institute, Nakhon Ratchasima, Thailand, and the X-ray wavelength, λ, was tuned at $\lambda = 1.55$ Å.

RESULTS AND DISCUSSION

Three IPC samples which are IPC-A, IPC-B, and IPC-C were used for this study and their mechanical properties were shown in Table I. IPC-B performs the highest impact-strength followed by IPC-C and IPC-A. For the tensile fracture properties, IPC-A shows the elongation at yield and at break remarkably higher than those of both IPC-B and IPC-C, while both tensile stresses at yield and at break are not significantly different for all samples. Because the melt flow index and EPR content, the parameters commonly used in industry, of these IPCs are in the same range, this comes to question what factors contribute to the

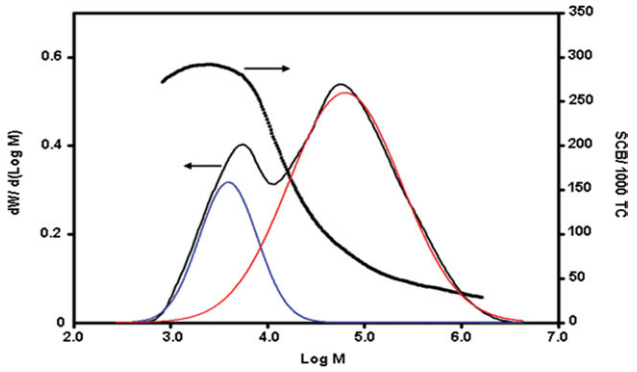

Figure 1. GPC profile of heptane-soluble fraction of IPC-A with its short chain branch (SCB) content per 1000 TC including Gaussian curve fit to separate LMW-PP (blue) and cEP_A (red). [Color figure can be viewed in the online issue, which is available at wileyonlinelibrary.com.]

observed difference in these mechanical properties. It has been widely accepted that IPC is a heterophasic (see earlier) material composed of three main components, that is, hPP, EPR, and cEP. Thus, they should play a vital role on the IPC properties and should be separated for further investigation.

To separate the components, the IPC pellets were dissolved in n-decane at 140°C and slowly cooled down to room temperature with the EPR, amorphous component, still remaining in solution. The EPR was precipitated in acetone to obtain clear rubber. The chemical structure of the EPR was verified by Fourier transform infrared (FTIR) spectroscopy with an absence of any crystalline PP and PE as confirmed by an absence of absorption peaks of crystalline PP and PE at 998 cm^{-1} and 841 cm^{-1}, and at 730 cm^{-1}, respectively. Absorption peaks at 973 cm^{-1} and 720 cm^{-1} corresponding to amorphous PP and methylene chain (—$(CH_2)_n$—, $n > 5$), respectively, were clearly seen [see Supporting information, Figure S1(a)].[13,20] Furthermore, thermal behavior of the amorphous material was also confirmed as seen by a flat line in the DSC thermogram [Supporting information, Figure S1(b)]. To separate the hPP, the decane-insoluble fraction was further extracted in heptane via soxhlet extraction for 5 h. A heptane-insoluble fraction or hPP was washed in acetone several times before drying at 110°C. The FTIR spectrum shows strong absorption peaks at 998 cm^{-1} and 841 cm^{-1} with no observed peak at 720 cm^{-1} (Supporting information, Figure S2). This confirms the presence of crystalline PP and absence of PE. The heptane-soluble fraction consisted of two main components: LMW-PP and cEP, as evidenced by its GPC profile which a clearly observed bimodal distribution is shown in Figure 1. An IR-detector equipped GPC revealed the SCB frequency of 300 branches in 1000 total carbon (TC) for the first peak (lower molecular weight) which is close to the value of hPP, ~333 SCB/1000 TC (one methyl group for every three carbons in its repeating unit). This confirms that the first peak contributes to LMW-PP and the second one might be cEP. This result was observed in all IPC samples (Supporting information, Figures S3 and S4). To our knowledge, cEP cannot be completely separated by chemical separation techniques. Thus, the cEP peak was separated mathematically by using a Gaussian-curve fit on the GPC data (Figure 1) used to recalculate several molecular parameters, such as M_w; homo-PP, homo-PE, and rEP contents in cEP. This separation procedure was applied to all IPC samples. An abbreviation of IPC components for each sample was as followed: EPR_A, hPP_A, and cEP_A for EPR, hPP, and cEP of IPC-A, respectively, and this abbreviation has been applied for all IPC samples.

Table II shows that the hPP, EPR, and cEP contents of all IPC samples are not significantly different. Thus, the effect of the component contents can be ignored. Therefore, the molecular characteristics such as M_w and EP distribution of each component need to be focused in detail.

M_w, M_n, and polydispersity index of hPP, EPR, and cEP for all IPC samples are shown in Table III. The M_w values for hPP and EPR are not dramatically different between samples and fall in the range 215,000–216,000 g/mol and 323,000–326,000 g/mol, respectively. Furthermore, for the hPP matrices, crystal structures directly affecting the impact strength of IPC were characterized by WAXD as shown in Supporting information, Figure S5. Only α-phase crystals with the same 2θ values were observed for all IPC samples. For the EPR, triad sequences (PPP + PPP_x, EEE + EEE_x, PEP + EPE, and PPE + EEP) are also in the same range in all samples (Table IV). These suggest that the main components, i.e. hPP and EPR, are not different for all IPC samples, thus it is worth focusing on the cEP component. The M_w value of cEP_A, ~176,000 g/mol is slightly higher than that of cEP_B and cEP_C which are both ~160,000 g/mol. However, the amount of homo-PP segment of cEP_A is almost twice as high as that of cEP_B and cEP_C (Table IV). The amount of homo-PE and rEP segments in cEP_A is remarkably

Table II. Content of Each IPC Components; hPP, EPR, and Heptane-Soluble Fraction Used for Calculating cEP and LMW-PP Contents by Gaussian Fitting

	Component content			
			Content of heptane-soluble fraction	
Samples	hPP content (% wt.)	EPR content (% wt.)	cEP content[a] (% wt.)	LMW-PP[a] content (% wt.)
IPC-A	80.35 ± 0.43	10.82 ± 0.23	4.76 ± 0.28	4.07 ± 0.28
IPC-B	79.45 ± 0.08	12.45 ± 0.13	4.15 ± 0.19	3.95 ± 0.19
IPC-C	82.80 ± 0.45	11.18 ± 0.94	3.8 ± 0.55	2.2 ± 0.55

[a]Calculated from Gaussian fitting of GPC profiles.

Table III. M_n, M_w, and polydispersity index of hPP, EPR, and cEP Components for IPC Samples

Molecular weight and PDI	Samples								
	hPP_A	hPP_B	hPP_C	EPR_A	EPR_B	EPR_C	cEP_A[a]	cEP_B[a]	cEP_C[a]
M_n (g/mol)	55,755	51,440	46,300	58,015	57,165	56,715	59,199	60,659	48,225
M_w (g/mol)	215,850	216,150	215,600	336,750	323,850	323,100	176,614	157,013	160,216
PDI	3.88	4.21	4.66	5.81	5.67	5.70	2.98	2.59	3.32

[a]Calculated from Gaussian-fitting peaks of cEP_x.

lower than that of cEP_B and cEP_C as evidenced by NMR. DSC results also confirm this. DSC thermograms show two ranges of endothermic peaks during heating scans [Figure 2(D–F)]. The multiple peaks ranging between 130 and 150°C contribute to the crystalline melting of LMW-PP and homo-PP segments, and the peak at ~117°C with a broad shoulder corresponds to the crystalline melting of homo-PE segments with various segmental lengths. The result clearly shows that the enthalpy of fusion for homo-PE of cEP_A is relatively small compared to that of cEP_B and cEP_C. It should be note that, for the endothermic peaks corresponding crystalline melting of PP in range 130–150°C, three peaks are clearly observed in cEP_A while only two peaks are seen in cEP_B and cEP_C. This can be implied that homo-PP segment of cEP_A might have variety of segmental length which results in forming various crystal sizes. In cooling scan, the exothermic peaks at ~100°C and 110°C contribute to the crystallization of PE and PP segments, respectively and [Figure 2(A–C)] also shows the same result. In addition, to clarify the segmental length of homo-PE in detail, SSA experiments were conducted. SSA is a technique that allows polymer segments which have the same uniform structure, such as similar composition and linear segmental lengths, to be crystallized in the same lamellar crystal. An average lamellar thickness (l_i) can be calculated by the Thomson-Gibb equation [eq. (1)].[21] Teng et al. have evaluated the lengths of linear segments of branched PE represented by l_i where the heat of fusion of a particular melting peak is directly related to the population of the corresponding crystal [eq. (2)]. However, the length of linear PE should be larger than the l_i value due to the presence of folded chains, thus this concept should be referred to as semiquantitative characterization as mentioned in their work.[22] In our case, the length of homo-PE segments can be approximately represented by l_i and its semiquantitative amount (Q_i) is evaluated by the following equations:

$$l_i = \frac{2\sigma Tm^0}{\Delta H_v (Tm^0 - Tm_i)} \quad (1)$$

$$Q_i = \frac{\rho_c \Delta H_i}{14.03 \Delta H_v} \cdot \frac{0.2534}{2l_i} = \frac{0.2534 \rho_c \Delta H_i (Tm^0 - Tm_i)}{56.12 \sigma Tm^0} \quad (2)$$

where σ is the lamellar surface free energy (70×10^{-3} J/m^2) and Tm^o is the equilibrium melting temperature (146°C for PE). ΔH_v is the enthalpy of fusion for a repeating unit (288×10^6 J/m^2 for CH_2) and Tm_i is the melting temperature of each endothermic peak. ρ_i is the density of the crystal (1 g/cm^3 for PE).[22] Figure 3(A) shows DSC thermograms collected via the SSA technique showing two series of peaks in the temperature ranges; 163–130°C and 125–60°C. The higher temperature-range peaks might contribute to LMW-PP and homo-PP segments while the lower temperature-range ones correspond to the crystalline melting of homo-PE segments. Figure 3(B) reveals that the quantities of homo-PE segments of cEP_B and cEP_C with lengths greater than 2 nm are clearly higher than that of cEP_A while there is no observed difference between segments shorter than 2 nm. This confirms that cEP_A has a lower content of long homo-PE segments compared to cEP_B and cEP_C.

At this point, from the NMR, GPC, and DSC results, we can conclude that the main differences in microstructure between the studied IPC samples are: (i) M_w of cEP_A is slightly higher than that of cEP_B and cEP_C, (Table III), (ii) cEP_A has a smaller content and shorter length of homo-PE segment than that of cEP_B and cEP_C [Table IV and Figure 3(B)], and (iii) cEP_A has

Table IV. E-P Triad Distribution Determined by ^{13}C NMR of EPR and cEP Components for IPC Samples

E-P triad	Sample					
	EPR_A (% mol)	EPR_B (% mol)	EPR_C (% mol)	cEP_A[a] (% wt.)	cEP_B[a] (% wt.)	cEP_C[a] (% wt.)
PPP + PPP_x	16.9	13.6	13.3	44.4	16.8	18.5
EEE + EEE_x	7.6	10.0	10.5	28.5	42.9	39.4
PEP + EPE	26.6	26.7	26.4	27.1[b]	40.3[b]	42.1[b]
PPE + EEP	48.9	49.6	49.8	-	-	-

[a]Corrected by weight fraction of LMW-PP.
[b]rEP content in cEP_x.

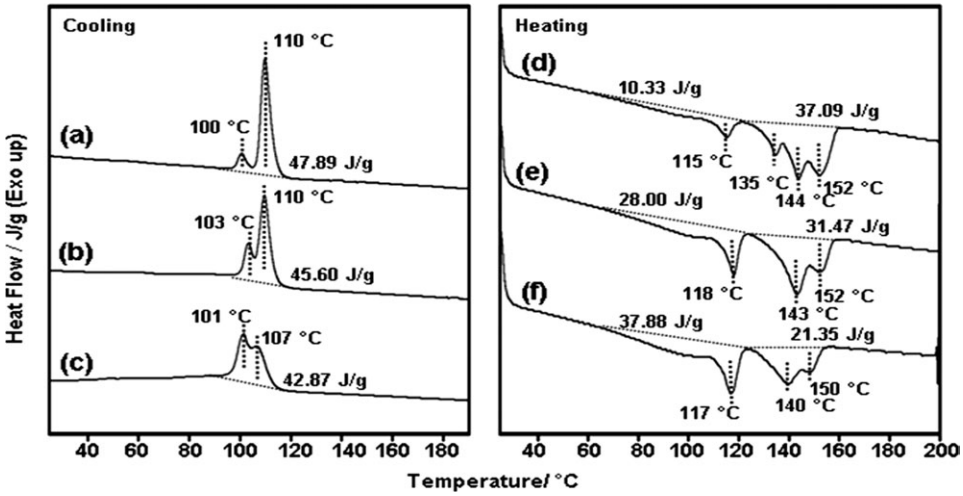

Figure 2. DSC profiles in cooling scan of: (A) cEP_A, (B) cEP_B, and (C) cEP_C, and in second heating scan of: (D) cEP_A, (E) cEP_B, and (F) cEP_C.

smaller content of rEP segment than those of cEP_B and cEP_C. These may be the factors that lead to the observed differences in mechanical properties.

For the heterophonic materials, such as IPC, phase morphology is an important issue which strongly affects their mechanical properties. In Figure 4, SEM micrographs of cryofractured IPC samples, taken after the removal of EPR by etching in toluene, show the dispersion of EPR pores in hPP. The diameter of each pore should be close to or a little larger than that of an EPR droplet, therefore the EPR diameter and its distribution can be evaluated by averaging the pore diameter. The result shows that the EPR-droplet diameter of IPC-A is smaller, ~0.53 μm [Figure 4(B)], compared to those of IPC-B and IPC-C which are ~0.65 μm [Figure 4(D, F)]. Furthermore, EPR droplets of IPC-A [Figure 4(A)] seem to be more uniformly dispersed in hPP compared to IPC-B and IPC-C [Figure 4(C, E)]. This might be due to a higher content of long homo-PP segments of cEP_A than those of cEP_B and cEP_C. This possibly promotes the compatibility between the EPR droplets and hPP matrix, which in turn strongly influences the elongation at break during the tensile fracture of the IPC.

To understand the fracture behavior of the IPC, the fractured specimens from both tensile and impact tests were examined. For the tensile fractures, SEM micrographs [Figure 5(B–D)] of selected zones of the fractured specimen [Figure 5(A)] show that microvoids along the stretching direction (SD) are clearly observed in IPC-B [Figure 5(C)] and IPC-C [Figure 5(D)]; however, only faint microvoids are observed in IPC-A [Figure 5(A)]. It is important to note that these microvoids are traces of inhomogeneous fracture, which will be discussed later. For the impact fractures, Figure 6(A) shows a specimen after impact testing with the fracture areas shown in the SEM micrographs [Figure 6(B–D)]. In the case of IPC-A [Figure 6(B)], the EPR droplets, distributed in the matrix, are clearly seen while just a few droplets are noticed in IPC-B [Figure 6(C)] and IPC-C [Figure 6(D)].

We now come to the point of how the cEP microstructure is related to the tensile and impact resistances of the IPCs. The answer might come from the early stages of the heterogeneous phase-formation, which occurs after the melted IPC is solidified. For a better understanding, schematic models representing cEP structures and EPR droplets are shown in Figure 7. It should be noted that the cEP is understood to be a mixture of EP copolymers with various EP compositions and distributions, such as homo-PE and homo-PP segmental copolymers with rEP segments, and EP block copolymers with a variety of block or

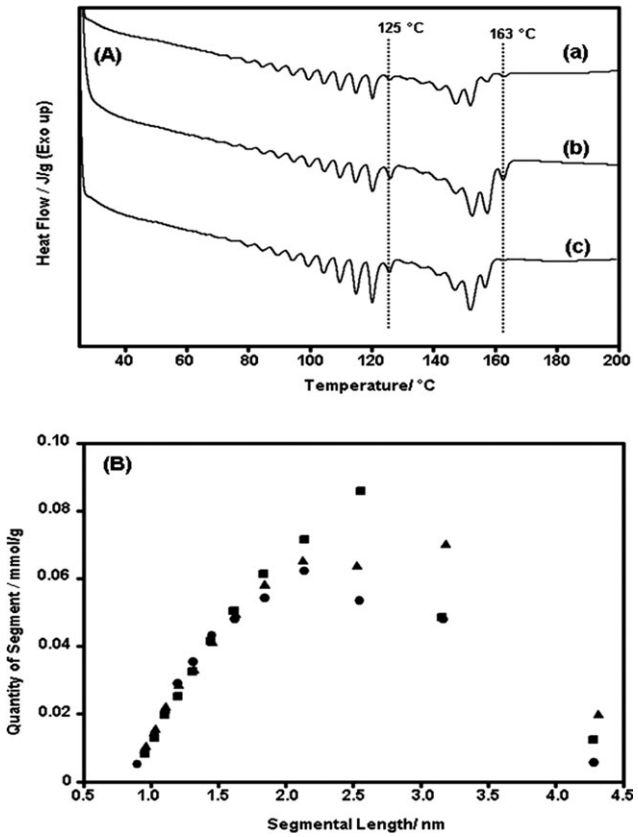

Figure 3. (A) SSA-DSC thermograms of: (a) cEP_A, (b) cEP_B, and (c) cEP_C; (B) length distribution of homo-PE segments of cEP_A (●), cEP_B (▲), and cEP_C (■).

Applied Polymer SCIENCE

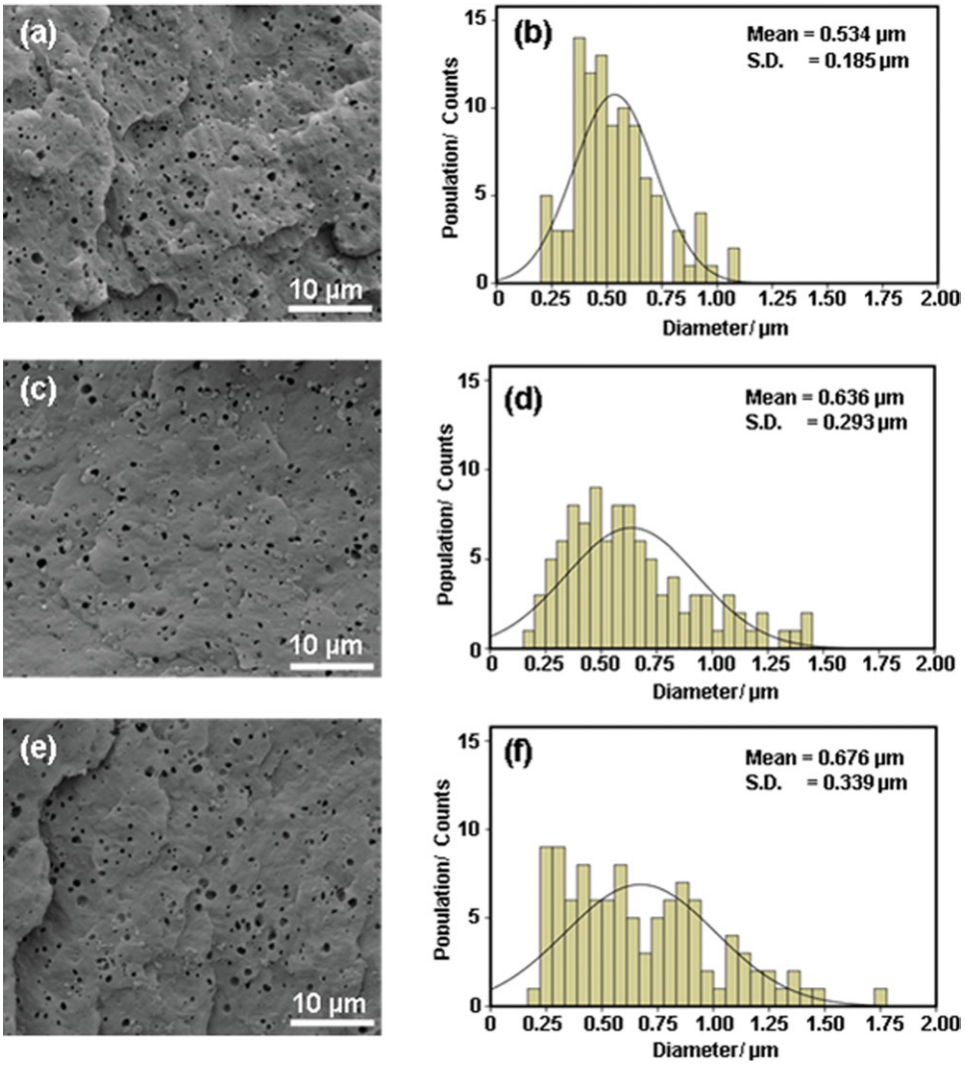

Figure 4. SEM micrographs of cryo-fractured tensile specimens of: (A) IPC-A, (C) IPC-B, and (E) IPC-C after etching in xylene, and their diameter distribution of EPR droplets for: (B) IPC-A, (D) IPC-B, and (E) IPC-C, respectively. [Color figure can be viewed in the online issue, which is available at wileyonlinelibrary.com.]

segmental lengths. However, to simplify this, two types of segmental copolymers which are PE-rich and PP-rich were selected to represent the cEP. It is important to note that PE-rich and PP-rich copolymers are the segmental copolymer contains high content of homo-PE and homo-PP, respectively. PP-rich segmental copolymers of IPC-A compose of long homo-PP segment. It is possible that it forms an EPR droplet containing a thick PP-rich layer at the EPR-hPP interphase which its long homo-PP segments can be co-crystallized with hPP matrix as reported by Song et al.[18] This leads to a good compatibility between the EPR droplet and hPP matrix as evidenced by the smaller EPR-droplet diameter and its good distribution [Figure 4(A, B)]. In the case of IPC-B and IPC-C, their PP-rich segmental copolymers which comprise of short homo-PP segments can form only thin PP-rich layers at the EPR-hPP interphase of which small portions of the homo-PP segment of cEP can be co-crystallized. However, the PE-rich core formed via a self-assembly from the homo-PE segment of the PE-rich segmental copolymers might be smaller in IPC-A due to smaller content and shorter length of homo-PE segment comparing with those in IPC-B and IPC-C. From these model structures, mechanisms related to the role of the cEP structure on the mechanical properties can be proposed.

For the tensile fracture, when the IPC is subjected to the stretching stress, the lamellar crystals of the hPP are deformed via at least three modes; inter-lamellar slip, inter-lamellar separation, and stack rotation in an amorphous matrix.[23] After the yield point, permanent deformation takes place due to voids appearing in the amorphous matrix. Beyond this point, the material elongation is dominated by the EPR phase. The stress is transferred to the EPR droplet, which is deformed along the SD. This causes a delayed rupture of the material under the tensile stretching. However, at a certain stress level, there are mainly two mechanisms for deterioration of the EPR droplet.[24] The first one is debonding if the adhesion between EPR and hPP phases is low, the second is a void forming inside the EPR droplet, so-called

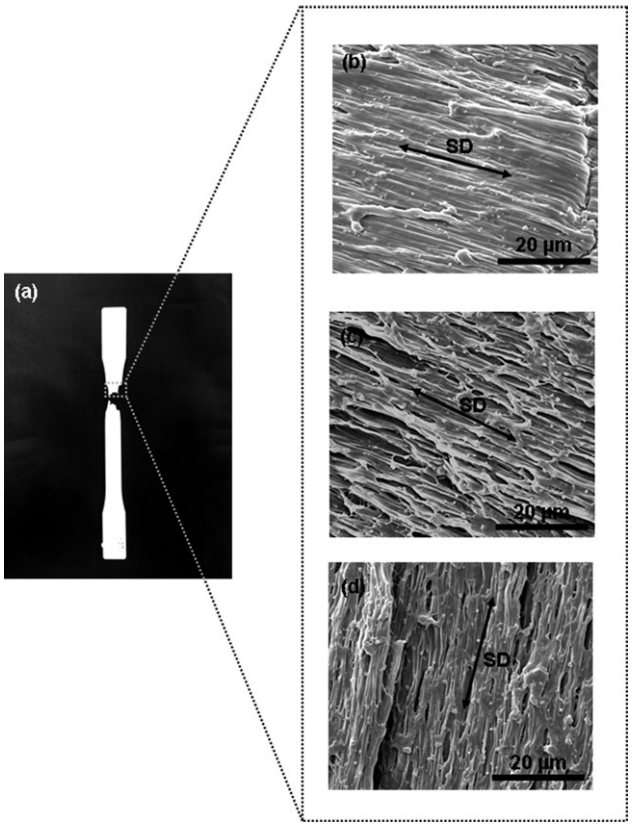

Figure 5. (A) Photograph of tensile fractured specimen, and SEM micrographs of fractured areas of (B) IPC-A, (C) IPC-B, and (D) IPC-C.

cavitation, at large strains if the phase adhesion is high enough to avoid debonding. Finally, the crystalline hPP matrix is broken as the material ruptures. In our cases, the EPR droplets still have been observed in all fractured samples which suggest that the debonding mechanism might be dominant [Figure 5(A–D)]. The results suggest that, in the case of IPC-A, the long homo-PP segments with high M_w of cEP promote phase adhesion causing a delayed debonding of the EPR by elongating the EPR droplets along the SD (Figure 8). Subsequently, in the cases of IPC-B and IPC-C, the debonding occurs during the early stages of stretching due to lower phase adhesion which is evidenced by the clearly observed microvoids [Figure 5(C, D)]. This might be responsible for the remarkably high elongations at break for IPC-A over IPC-B and IP-C.

For the impact fracture, EPR phase plays a crucial role in the material toughening by absorbing the impact energy. Thus, a toughness improvement is related to how the energy can be effectively transferred to the EPR phase. The IPC is tougher when the fracture front preferentially passes through the EPR droplet. In other words, the toughness of the IPC is relatively low if the fracture front propagates in the matrix or at the EPR-hPP interphase (or debonding).[25] In our cases, SEM results showed that EPR droplets were still observed in IPC-A suggesting that the fracture front passed preferentially through the EPR-hPP interphase or a shallow region of EPR droplet. In the cases of IPC-B and IPC-C only, a few EPR droplets have been revealed suggesting that the fracture front might propagate through the EPR droplet. Furthermore, IPC-B and IPC-C also have a larger rigid PE core than IPC-A as mentioned above. These might be the reasons why the impact strengths of IPC-B and IPC-C are higher than IPC-A. However, as discussed previously, IPC-A might have a better phase adhesion than IPC-B and IPC-C. Thus, it is surprising that the fracture front passed along the EPR-hPP interphase and not through the EPR droplet for the IPC-A. It is important to mention that the amounts of homo-PE and rEP segments in cEP_B and cEP_C are higher than that of cEP_A which might make them more effective at transferring energy from the hPP matrix to the core of the EPR droplets. In other words, in the case of IPC-A, the propagation of the fracture front proceeded through only a shallow region of the EPR shell while, in the case of IPC-B and IPC-C, it passed through almost the center or deeper region of the EPR droplet as shown in schematic model in Figure 9.

CONCLUSIONS

This work showed the microstructure elucidation for each IPC component in detail, especially cEP which homo-PP, homo-PE, and rEP segments were clearly clarified. The result showed that, besides EPR and hPP components, cEP plays a major role on the IPC properties. The results indicated that the content of the homo-PP segment in cEP directly affects the tensile resistance

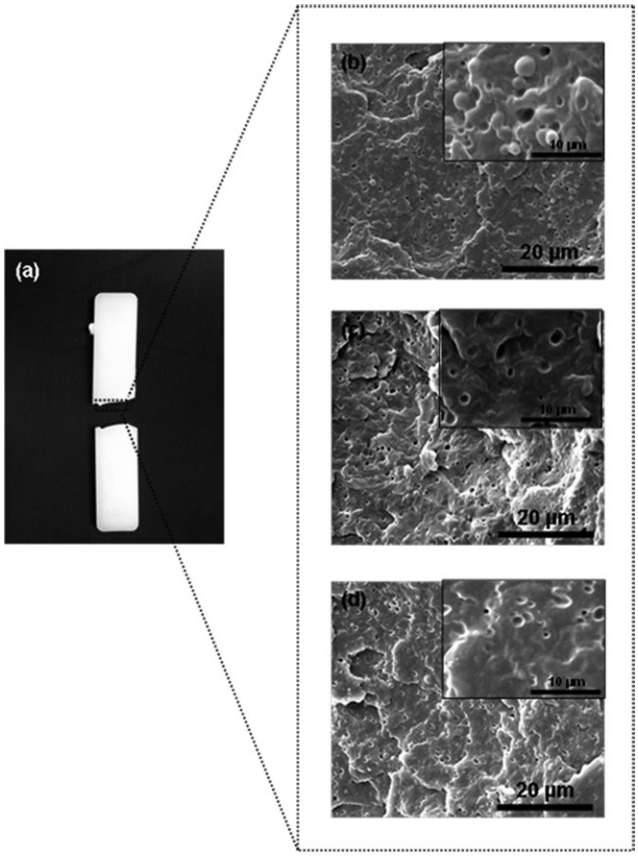

Figure 6. (A) Photograph of impact fractured specimen, and SEM micrographs of fractured areas of (B) IPC-A, (C) IPC-B, and (D) IPC-C including their high-magnified expansion.

Applied Polymer SCIENCE

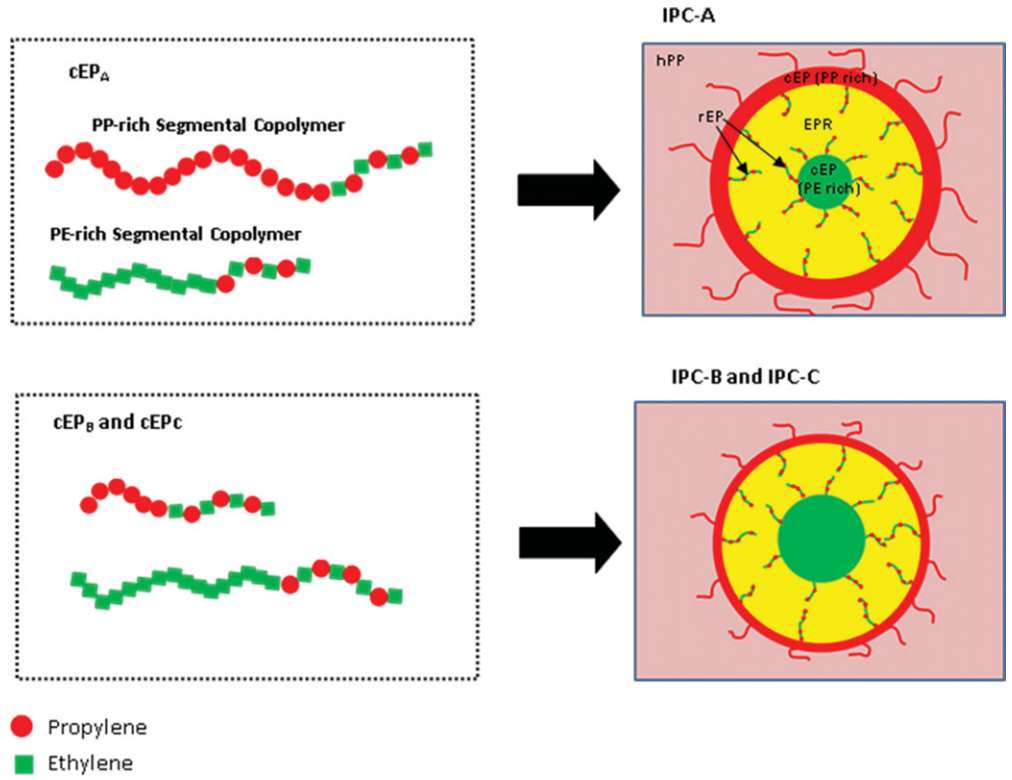

Figure 7. Schematic model represented cEP structures and heterophasic morphologies of IPC-A; and IPC-B and IPC-C. [Color figure can be viewed in the online issue, which is available at wileyonlinelibrary.com.]

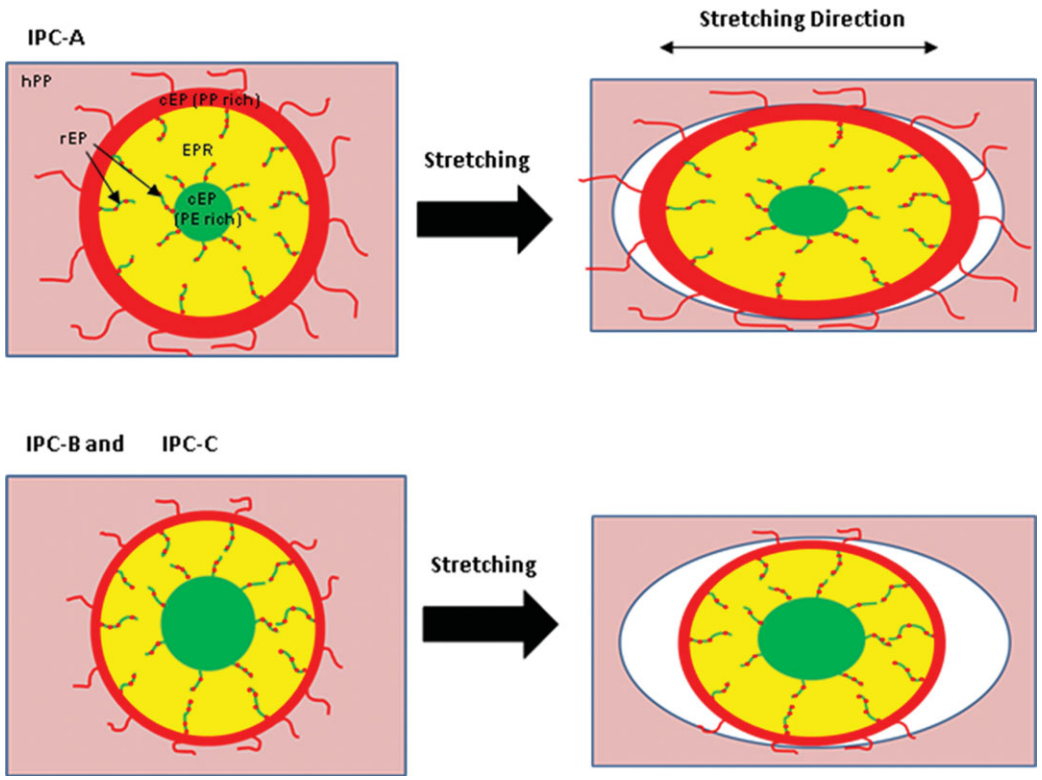

Figure 8. Schematic model illustrating mechanism proposed for tensile fracture of IPC-A; and IPC-B and IPC-C. [Color figure can be viewed in the online issue, which is available at wileyonlinelibrary.com.]

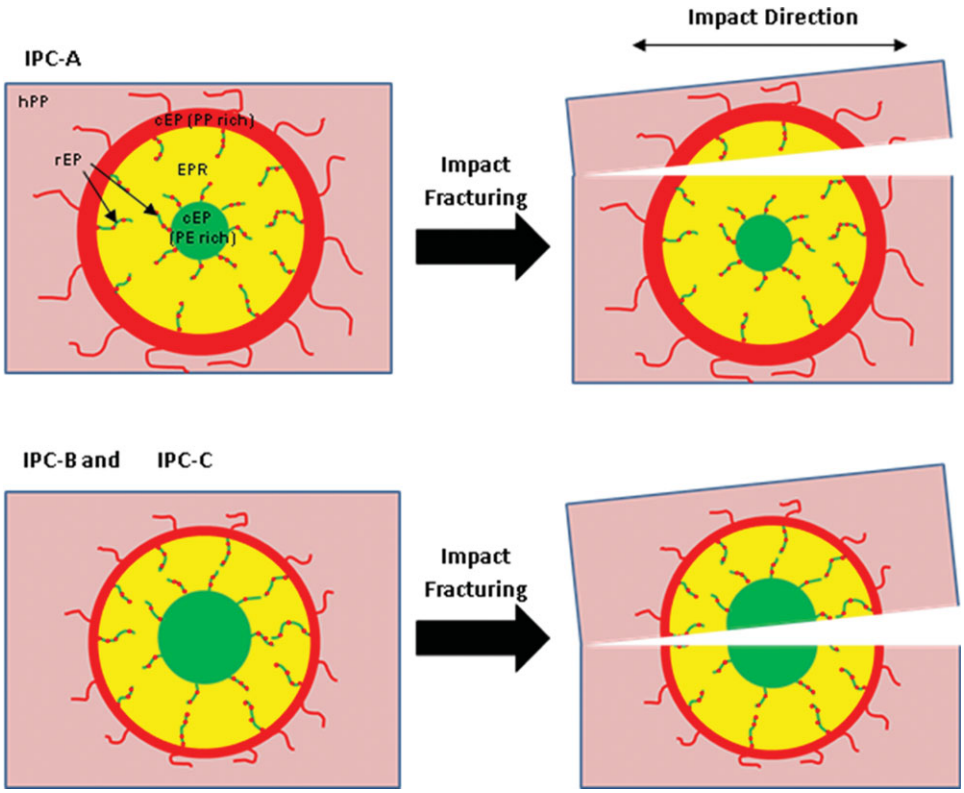

Figure 9. Schematic model illustrating mechanism proposed for impact fracture of IPC-A; and IPC-B and IPC-C. [Color figure can be viewed in the online issue, which is available at wileyonlinelibrary.com.]

while the homo-PE segment contributes to the impact strength. It leads to the proposed mechanism that cEP with high content of long homo-PP segments might co-crystalize with the hPP matrix which delays the debonding of the EPR droplet. Thus, the microvoids should form during the later stages of tensile fracture which prolongs the material breaking. For the impact fracture, cEP with a high content of rEP and long homo-PE segments might form a large PE-rich core covered by a thick EPR shell. This structure provides rigidity and promotes the propagation of a fracture front through the center or deep region of an EPR droplet which in turn enhances the impact resistance of the IPC.

ACKNOWLEDGMENTS

The authors would like to express their gratitude to Thai Polyethylene Co., Ltd., (TPE) for the financial support and Thai Polypropylene Co., Ltd., (TPP) for the IPC samples. The authors acknowledge the product-development-support (PDS) team for supporting the experiments. Gratitude is also shown towards Miss Nisarat Taweewan and Ms. Namoiy Wisatat, RD Center Rayong, Thai Plastic and Chemical Co., Ltd (TPC) for supporting the SEM observations. The authors would also like to acknowledge Dr. Jan Kratochvila (POLYMER INSTITUTE BRNO, Czech Republic) for his advice on NMR calculations and Dr. Daniel Suckley (TPE) for his comments concerning the content. Finally, the author (W.R.) would like to thank Miss Kanyanat Narkchamnan who contributed to the calculation revision.

REFERENCES

1. Pasquini, N. In Polypropylene Handbook, 2nd ed.; Hanser Verlag, Cincinnati, Ohio, **2005;** p 307–317.
2. Rosa, C. D.; Auriemma, F. *J. Am. Chem. Soc.* **2006,** *128*, 11024.
3. Premphet, K.; Horanont, P. *Polymer* **2000,** *41*, 9383.
4. Greco, R.; Mancarella, C.; Ragosta, G.; Yin, J. *Polymer* **1987,** *28*, 1929.
5. McEvoy, R. L.; Krause, S. *Macromolecules* **1996,** *29*, 4258.
6. Zhang, X. F.; Xie, F.; Zhang, Y.; Zhang, Y. X.; Zhou, W. *Eur. Polym. J.* **2002,** *38*, 1.
7. Yijian, L.; Marchand, G. R.; Hiltner, A.; Bear, E. *Polymer* **2011,** *52*, 1635.
8. Mairabella, F. M. *Polymer* **1993,** *34*, 1729.
9. Xu, J. T.; Feng, L. X. *Polymer Int* **1998,** *47*, 433.
10. Cai, H. J.; Luo, X. L.; Chen, X. X.; Ma, D. Z.; Wang, J. M.; Tan, H. S. *J. Appl. Polym. Sci.* **1999,** *39*, 6589.
11. Dong, Q.; Wang, X.; Fu, Z.; Xu, J.; Fan, Z. Q. *Polymer* **2007,** *48*, 5905.
12. Zhu, H.; Monrabal, B.; Han, C. C.; Wang, D. *Macromolecules* **2008,** *41*, 826.
13. Xue, Y.; Fan, Y.; Bo, S.; Ji, X. *Eur. Polym. J.* **2011,** *47*, 1646.
14. Tian, Z.; Gu, X. P.; Wu, G. L.; Feng, L. F.; Fan, Z. Q.; Hu, G. H. *Ind. Eng. Chem. Res.* **2011,** *50*, 5992.
15. Zhang, C.; Shangguan, Y.; Chen, R.; Wu, Y.; Chen, R.; Zheng, Q.; Hu, G. *Polymer* **2010,** *51*, 4969.

16. Luo, F.; Xu, C.; Wang, K.; Deng, H.; Chen, F.; Fu, Q. *Polymer* **2012,** *53*, 1783.
17. Tan, H.; Li, L.; Chen, Z.; Song, Y.; Zheng, Q. *Polymer* **2005,** *46*, 3522.
18. Song, S.; Feng, J.; Wu, P.; Yang, Y. *Macromolecules* **2009,** *42*, 7067.
19. Song, S.; Feng, J.; Wu, P.; Yang, Y. *Polymer* **2010,** *51*, 5267.
20. Drushel, H. V.; Iddings, F. A. *Anal. Chem.* **1963,** *35*, 28.
21. Müller, A. J.; Arnal, M. L. *Prog. Polym. Sci.* **2005,** *30*, 559.
22. Teng, H. X.; Shi, Y.; Jin, X. G. *J. Polym. Sci. Part B: Polym. Phys.* **2002,** *40*, 2107.
23. Galeski, A. *Prog. Polym. Sci.* **2003,** *28*, 1643.
24. Zebarjad, S. M.; Bagheri, R.; Sayed Reihani, S. M.; Lazzeri, A. *J. Appl. Polym. Sci.* **2003,** *90*, 3767.
25. Zebarjad, S. M.; Lazzeri, A.; Bagheri, R.; Sayed Reihani, S. M.; Frounchi M. *Mater. Lett.* **2003,** *57*, 2733.